

AIRFRAME HEALTH MONITORING ON THE BAE SYSTEMS HAWK T1A JET TRAINER

Gabriele Dessena [1], Marco Civera [2], Elia P. Mottola[3] & Oscar E. Bonilla-Manrique [4]

[1]Department of Aerospace Engineering, Universidad Carlos III de Madrid, Avenida de la Universidad 30, Leganés, 28911, Madrid, Spain
[2]Department of Structural, Geotechnical and Building Engineering, Politecnico di Torino, Corso Duca degli Abruzzi 24, 10129, Turin, Italy
[3]Department of Mechanical and Aerospace Engineering, Politecnico di Torino, Corso Duca degli Abruzzi 24, 10129, Turin, Italy
[4]Electronic Technology Department, Universidad Carlos III de Madrid, Avenida de la Universidad 30, Leganés, 28911, Madrid, Spain

Abstract

Scheduled maintenance frameworks in aerospace constrain operational availability and may fail to capture structural degradation occurring between inspection cycles. Vibration-based structural health monitoring (SHM) offers a route to condition-based maintenance, yet full-airframe validation on operational-scale structures remains rare. This work applies modal analysis to a full-scale BAE Systems Hawk T1A jet trainer, using mode shape correlation as the primary damage indicator across 19 multiple-input, multiple-output ground vibration test configurations spanning six damage scenarios and three incremental mass levels. Modal parameters are extracted via the improved Loewner Framework, with natural frequency agreement within 1% for 25 of 31 identified modes relative to a published reference. A constrained linear regression of MAC values relative to the healthy baseline yields slopes of -0.0807 (all scenarios) and -0.0828 (single-location scenario), confirming consistent damage sensitivity across locations. Four modes at 97.6, 106.8, 125.6, and 151.3 Hz satisfy a strict monotonicity criterion, with tracked MAC values ranging from 0.9581 to 0.2255, providing a differential basis for both detection and severity assessment. These results support the adoption of mode shape-based SHM strategies in aerospace and other safety-critical industries.

Keywords: Structural Health Monitoring, Airframe, Ground Vibration Testing, Modal Parameter Identification, Loewner Framework, Modal Assurance Criterion.

1. Introduction

Traditional aircraft design and certification practices are governed by safe-life and damage-tolerance frameworks, which mandate predetermined maintenance intervals and inspection cycles that directly constrain the operational availability of an aircraft [1]. Scheduled inspections may be required both at the global airframe level [2] and at the local component level. The combination of these requirements produces scenarios in which components are replaced or inspected despite remaining structurally sound, or in which structural degradation arises between inspection cycles under specific operational conditions, as illustrated by the Aloha Airlines Flight 243 accident [3], where a Boeing 737-200 operating short-hop routes experienced a severe non-catastrophic fuselage blowout.

Structural Health Monitoring (SHM) offers a potential route to rationalise maintenance scheduling, thereby improving operational planning and, ultimately, mission effectiveness or commercial profitability. In the context of vibration-based SHM, modal parameters – natural frequencies (ω_n), damping ratios (ζ_n), and mode shapes ($\boldsymbol{\phi}_n$) – are frequently adopted as damage indicators owing to their

https://doi.org/10.71945/icas2026_0706

direct relationship with the structural mass and stiffness distributions, as well as their possibility to be extracted from vibration response data [4]. These parameters serve complementary roles in damage characterisation. ω_n are particularly suitable for assessing damage severity, although their sensitivity to environmental and operational variability limits their reliability for localisation [5]. When used successfully, they have been applied to the SHM of civil structures such as masonry bridges using single-input, multiple-output (SIMO) data [6]. $\boldsymbol{\phi}_n$, in contrast, are better suited to damage localisation through comparison against a baseline, and have been used in two-step detection procedures for beam-like structures [7]. ζ_n are rarely adopted as standalone damage indicators due to their strong dependence on non-structural factors, which renders it difficult to attribute damping changes unambiguously to structural degradation [8].

Beyond these classical strategies, a growing body of literature has addressed vibration-based SHM in the context of civil infrastructure and rotating machinery, with particular attention to uncertainty quantification, noise robustness, and operational variability. Bridges [9] and wind turbines [10] have received substantial attention. In addition, more recent developments include neural architectures informed by Cepstral coefficients for physical interpretability [11], operational modal analysis adapted to the time-periodic dynamics of wind turbine rotors [12], convolutional neural networks for damage classification under moving loads [13], and guided wave SHM enhanced with Gaussian mixture models for operational damage detection in aeronautical structures [14]. Nevertheless, no unequivocal solution for SHM exists at present, as most methods remain either insufficiently validated or not yet codified in national or international standards [15].

In aerospace and aeronautical engineering, the prevalent approach consists of detailed analyses of individual subsystems such as fuel pumps [16], blades [17], engine brackets [18], and spars [19], rather than complete or partial airframes, despite early efforts in space shuttle monitoring [20]. This focus on subsystems is partly a consequence of dataset availability: the majority of vibration-based SHM benchmarks rely on SIMO or output-only data, rather than multiple-input, multiple-output (MIMO) configurations. MIMO testing can provide access to modes not fully identifiable from single-input or output-only campaigns, such as out-of-plane-dominated modes in flexible wings [21], and this additional information is consequential for damage characterisation. The Z24 bridge case study illustrates this argument: the weakly excited lateral modes are the most difficult to identify [22], yet they were shown to be the most indicative of structural damage [23], which supports the premise that reliably identifying low-amplitude modes can materially improve the precision of vibration-based SHM.

This work addresses the gap between SHM at the subsystem level and monitoring of the complete airframe by applying modal MIMO analysis to a full-scale BAE Systems Hawk T1A jet trainer. The adopted SHM strategy is based on $\boldsymbol{\phi}_n$ correlation: a change in the $\boldsymbol{\phi}_n$ trajectory is interpreted as evidence of structural modification, and the spatial distribution of this deviation indicates its location [24]. The experimental data are drawn from the publicly available dataset produced by the Dynamics Research Group and Laboratory of Verification and Validation (LVV) at the University of Sheffield [25], which includes 216 MIMO ground vibration test configurations that span multiple damage scenarios, excitation types, and amplitude levels. Modal identification across all cases is performed using the improved Loewner Framework (iLF) [26]. To the authors' knowledge, this constitutes the first study of such scope on this dataset. Previous efforts have examined only subsets of modes and structural configurations [27, 28], or classified healthy and damaged scenarios solely on the basis of the time-domain response [29].

2. Materials and Methods

2.1 BAE Systems Hawk T1A Jet Trainer

The experimental data used in this work originate from a Ground Vibration Testing (GVT) campaign conducted on a full-scale BAE Systems Hawk T1A jet trainer at the LVV facilities of the University of Sheffield (Sheffield, UK) [25]. The aircraft, a decommissioned two-seat advanced trainer previously in service with the British Royal Air Force, is shown in Figure 1. The dataset[1] is described in full in

[1] Accessible at `https://orda.shef.ac.uk/articles/dataset/BAE_T1A_Hawk_Full_Structure_Modal_Test/24948549` via the Python API at `https://github.com/MDCHAMP/hawk-data`.

[25] and only the aspects directly relevant to this study are recalled below.



Figure 1 – BAE Systems Hawk T1A aircraft at the LVV in Sheffield, UK (retrieved from [25]).

A total of 216 MIMO test configurations are included, covering multiple structural states, excitation waveforms, and input voltage levels. The excitation system consists of five Tira^{TM} TV 51140-MOSP modal shakers paired with PCB Piezotronics^{TM} 208C02 force transducers (nominal sensitivity: 11.11 mVN^{-1}), one per surface: starboard wing, port wing, starboard horizontal stabiliser, port horizontal stabiliser, and vertical stabiliser. Response measurements are obtained from 85 PCB Piezotronics accelerometers — a mix of uniaxial and triaxial units — producing 91 independent acceleration channels. Their distribution across the aircraft frame is shown in Figures 2 to 4 and can be summarised as follows [25]:

1. Each wing is covered by two rows of uniaxial sensors on the upper surface (14 channels in total, running parallel to both edges) and a single row of seven on the lower one, totalling 21 channels per wing (Figure 2);
2. Ten uniaxial sensors are placed on each horizontal stabiliser, arranged in two rows of five sensors each on the upper surface only (Figure 3);
3. The vertical stabiliser carries 10 uniaxial sensors on its starboard face, split equally between the leading and trailing edges (Figure 3);
4. A sensitivity of 10 mVg^{-1} is common to all wing and stabiliser accelerometers;
5. Three triaxial accelerometers (100 mVg^{-1}) are positioned on the nose of the fuselage, at the cockpit station, and on the tail (Figure 4);
6. Four uniaxial units (100 mVg^{-1}) monitor the fuselage cross-section at mid-length, one on each face (Figure 4);
7. Six more uniaxial sensors (100 mVg^{-1}) cover the three landing gear assemblies, two per unit.

The triaxial reference accelerometer, placed on the laboratory floor in the original configuration, is not included in the current analyses. Strain gauges and environmental probes contribute to a total channel count of 139, but these other sensing devices are not considered for this study.
The cases selected for this study use white Gaussian noise (WGN) excitation at the lowest available voltage (0.1 V) in the full five-shaker MIMO configuration, bandlimited to 5–256 Hz at a sampling rate of $f_s = 2048$ Hz, keeping the structural response within the linear regime consistent with standard GVT practice [27]. Damage consists of localised mass additions at three span-wise positions on each wing, namely the root leading edge (xW_RLE), the centre trailing edge (xW_CTE), and the tip leading edge (xW_TLE), where xxW denotes either the port (PW) or starboard (SW) wing. Three incremental weights, M1 (254.3 g), M2 (616.8 g), and M3 (916.8 g), are used to simulate increasing

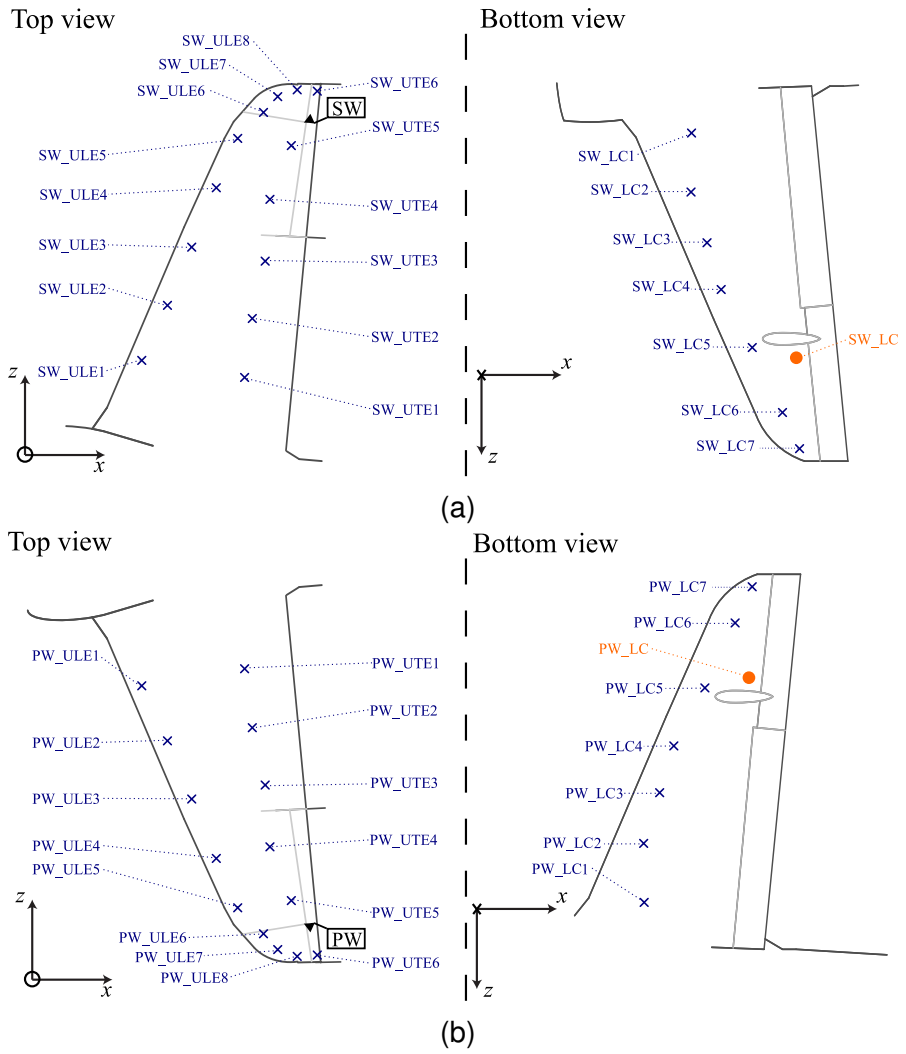


Figure 2 – BAE Systems Hawk T1A aircraft: sensor layout for the starboard (Figure 2a) and port wing (Figure 2b). Adapted from [25] (Note: the bottom-view sensor ordering in [25] runs tip-to-root).

damage severity at each position. The damage map for the port wing is shown in Figure 5; the starboard wing carries mass additions at the symmetric span-wise positions. The full set of cases considered is given in Table 1. Input scenario labels follow the dataset convention [25]: HS and DS denote the healthy and damaged structural states respectively, WN identifies the white Gaussian noise excitation, and the trailing index 01 corresponds to the lowest amplitude level (0.1 V).
Acceleration time series were recorded across all 91 output channels considered at a sampling frequency of $f_s = 2048$ Hz, with the input bandwidth spanning 5–256 Hz. Ten repeated acquisitions are available per test configuration [25].

2.2 Methodology

The identification process uses the mean (across the 10 test repetitions) FRF, calculated across the ten available repetitions per test condition. More specifically, the MIMO FRFs between each of the five force inputs and all 91 acceleration outputs are computed as H_1 estimators:

$$H_1(\omega) = S_{YX}(\omega) / S_{XX}(\omega), \tag{1}$$

where $S_{YX}(\omega)$ denotes the cross-spectral density between output and input, and $S_{XX}(\omega)$ the input auto-spectral density. A short-time Fourier transform with a Hann window, 16 384-sample segments, and 50% overlap is used to evaluate both quantities, following [25]. The H_1 formulation attenuates output-side noise, which would otherwise distort FRF valleys, whilst preserving phase content through the cross-spectral term [30].

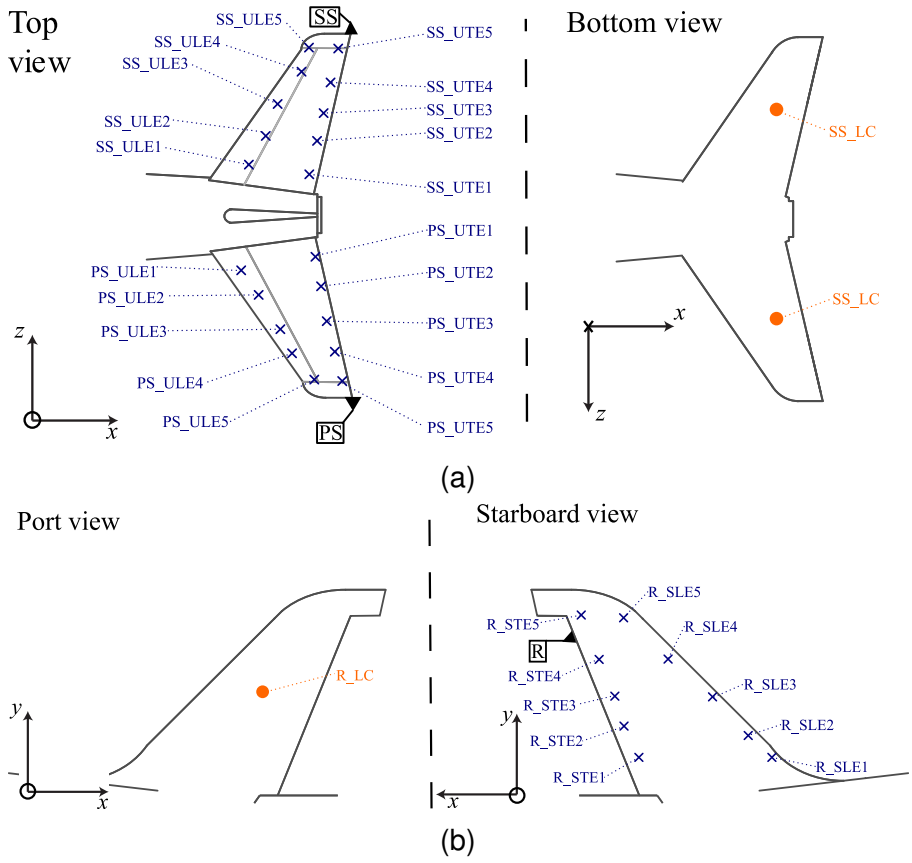


Figure 3 – BAE Systems Hawk T1A aircraft: sensor layout for the horizontal stabiliser (Figure 3a) and vertical stabiliser (Figure 3b). Adapted from [25].

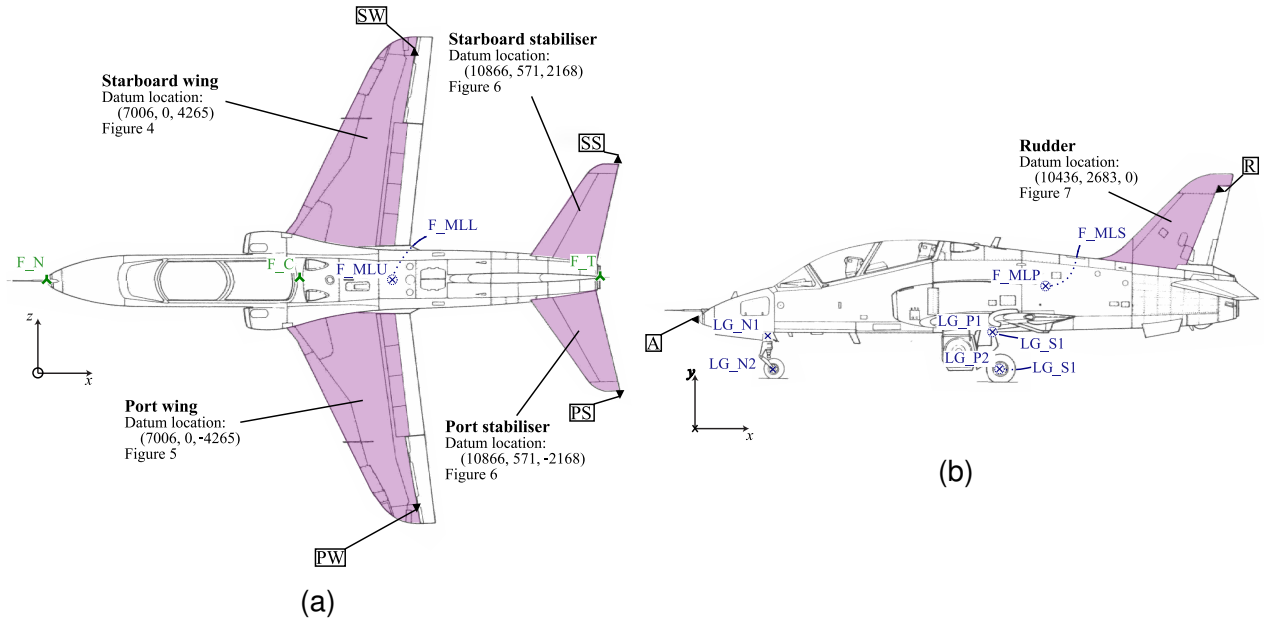


Figure 4 – Hawk T1A aircraft: sensor layout for the fuselage and landing gear, top view (Figure 4a) and port-side view (Figure 4b). Adapted from [25].

Modal parameters are extracted from the mean FRFs using iLF [26]. The iLF fits a linear time-invariant state-space realisation to frequency-domain data via tangential interpolation, recovering the modal parameters through eigenanalysis of the resulting system matrices. Stable physical poles are selected from stabilisation diagrams constructed across a range of model orders. All 19 cases in Table 1 are identified independently using identical settings, with the healthy baseline (HS_WN_01)

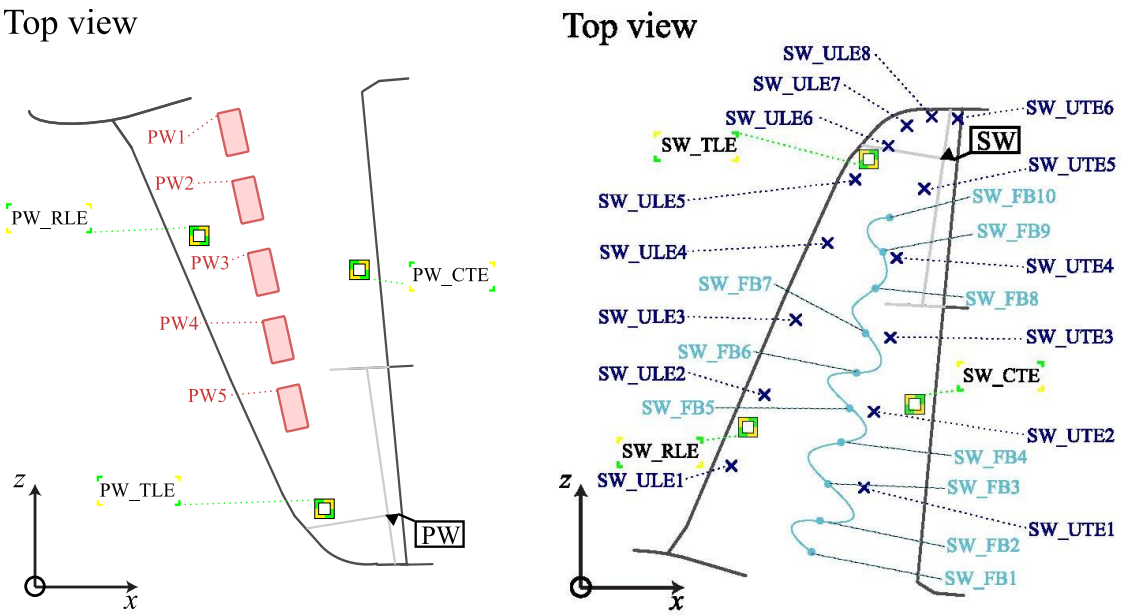


Figure 5 – Hawk T1A aircraft: mass addition positions on the port wing (PW_xxE, Figure 5a) and on the starboard wing (SW_xxE, Figure 5b). Adapted from [25].

Table 1 – BAE Systems Hawk T1A aircraft: test scenarios considered in this study. All cases use WGN excitation at Amplitude 1 in the full MIMO configuration. HS: healthy state; DS: damaged state; WN: white noise; 01: lowest amplitude level.

Case	Input scenario	Description
1	HS_WN_01	Healthy baseline
2	DS_WN_01	M1 at SW_CTE
3	DS_WN_01	M2 at SW_CTE
4	DS_WN_01	M3 at SW_CTE
5	DS_WN_01	M1 at SW_RLE
6	DS_WN_01	M2 at SW_RLE
7	DS_WN_01	M3 at SW_RLE
8	DS_WN_01	M1 at SW_TLE
9	DS_WN_01	M2 at SW_TLE
10	DS_WN_01	M3 at SW_TLE
11	DS_WN_01	M1 at PW_CTE
12	DS_WN_01	M2 at PW_CTE
13	DS_WN_01	M3 at PW_CTE
14	DS_WN_01	M1 at PW_RLE
15	DS_WN_01	M2 at PW_RLE
16	DS_WN_01	M3 at PW_RLE
17	DS_WN_01	M1 at PW_TLE
18	DS_WN_01	M2 at PW_TLE
19	DS_WN_01	M3 at PW_TLE

serving as the reference state against which all damaged configurations are compared.
The damage detection strategy is based on $\boldsymbol{\phi}_n$ correlation. A deviation in the $\boldsymbol{\phi}_n$ trajectory between the healthy and a given damaged state is interpreted as evidence of structural modification, and the spatial distribution of that deviation indicates its location [4]. The Modal Assurance Criterion (MAC) [31] condenses this comparison into a scalar index:

$$\mathrm{MAC}\left(\boldsymbol{\phi}_i, \boldsymbol{\psi}_j\right) = \frac{\left|\boldsymbol{\phi}_i^{\mathrm{T}} \boldsymbol{\psi}_j\right|^2}{\left(\boldsymbol{\phi}_i^{\mathrm{T}} \boldsymbol{\phi}_i\right)\left(\boldsymbol{\psi}_j^{\mathrm{T}} \boldsymbol{\psi}_j\right)} \tag{2}$$

where $\boldsymbol{\phi}_i \in \mathbb{R}^n$ and $\boldsymbol{\psi}_j \in \mathbb{R}^n$ are the i-th and j-th mode shapes respectively, and n is the number of measured degrees of freedom. A MAC value of unity shows perfect correlation, while any reduction represents a change in the mode-shape trajectory that is likely due to structural modification, such as damage.

For each healthy mode i, the corresponding damaged mode is identified by selecting the candidate j, within a frequency window around mode i, such that the MAC value is maximised, giving the tracked MAC for the damage state k:

$$\mathrm{MAC}_{\mathrm{tracked}}(i,k) = \max_j \mathrm{MAC}\left(\boldsymbol{\phi}_i, \boldsymbol{\psi}_j^{(k)}\right) \tag{3}$$

With three progressive mass levels available at each location (M1, M2, M3), it is possible to assess whether a mode responds monotonically to increasing damage severity. A mode is classified as a damage indicator if its tracked MAC decreases strictly across all three levels:

$$\mathrm{MAC}_{\mathrm{tracked}}(i,1) > \mathrm{MAC}_{\mathrm{tracked}}(i,2) > \mathrm{MAC}_{\mathrm{tracked}}(i,3) \tag{4}$$

The modes satisfying Equation (4) constitute the primary outcome of this study, as they represent $\boldsymbol{\phi}_n$ features with a reliable response to structural modification.

3. Results

The first step was to assess the quality of the iLF identification for the healthy baseline (HS_WN_01) against the values available in the literature. The reference is drawn from [26], where a MIMO iLF identification of the same aircraft was performed at an excitation amplitude of 0.4 V, resulting in the modal parameters of the healthy configuration. The present study operates at 0.1 V. Thus, minor discrepancies in both ω_n and ζ_n are expected, primarily due to the lower signal-to-noise ratio at reduced amplitude.

Table 2 presents the 31 modes identified for the healthy baseline alongside the corresponding reference values from [26] and the percentage differences in natural frequency ($\Delta f\,[\%]$) and damping ratio ($\Delta\zeta\,[\%]$).

The natural-frequency agreement between the two identifications is good for most modes ($f_n = \omega_n/2\pi$, in Hz): 25 of the 31 modes exhibit $|\Delta f_n| \leq 1\%$, and only modes 7, 8, 13, and 24 exceed 3%. These outliers are attributable to mode ordering ambiguities in the lower signal-to-noise ratio of the 0.1 V test, or to the genuine amplitude sensitivity of these modes. By contrast, the damping-ratio discrepancies are substantially larger, as expected: $|\Delta\zeta|$ ranges from below 3% (modes 6, 20, 32, 34, 36) to above 50% for mode 15, consistent with the known sensitivity of ζ_n estimates to excitation amplitude and noise floor [26]. Consequently, the modes with $|\Delta\zeta| > 40\%$ (14, 15, 16, 38) should be treated with caution as stand-alone damping-based damage indicators.

Figure 6 shows the first mode shapes, $\boldsymbol{\phi}_{1-3}$, from the reference identification [26], corresponding to the dominant low-frequency wing modes. Mode 1 (6.98 Hz) is a symmetric out-of-plane bending mode of both wings, with the maximum displacement at the port and starboard tips. Mode 2 (15.43 Hz) is an antisymmetric bending mode, with opposing tip deflections. Mode 3 (16.32 Hz) exhibits a combined bending–torsion character, visible in the span-wise twist of the wing surfaces. The present identification reproduces this ordering with $|\Delta f| \leq 1.05\%$ for all three modes, confirming that the iLF at 0.1 V correctly resolves the global low-frequency dynamics of the aircraft frame.

3.1 MAC-based damage assessment across all scenarios

The mode shapes $\boldsymbol{\phi}_n$ for all 19 cases are considered next. Figure 7 presents the MAC values of all identified modes with respect to the healthy baseline, obtained for all six damage scenarios and all three damage levels (19 total cases), together with a constrained linear regression of the form $y = ax + 1$, such that it passes through the point $(0, 1)$, consistent with the physical expectation that zero structural modification implies perfect $\boldsymbol{\phi}_n$ correlation.

As shown in Figure 7, the MAC response is not uniformly monotonic across all modes and scenarios: a subset of modes exhibits non-monotonic or weakly varying behaviour, reflecting their low sensitivity to the mass additions at specific locations. Nevertheless, the fitted regression slope is negative (-0.0807), confirming that, on average, $\boldsymbol{\phi}_n$ correlation with the healthy baseline degrades with

Table 2 – BAE Systems Hawk T1A aircraft: healthy state (HS_WN_01, Amplitude 1) versus MIMO reference from [26] (0.4 V input – HS_WN_04). Δf_n and $\Delta\zeta_n$ are percentage differences with respect to the reference values.

Mode	HS_WN_01		HS_WN_01 [26]	
	f_n [Hz]	ζ_n [%]	f_n [Hz]	ζ_n [%]
1	7.009	1.7648	6.976	2.7551
	$\Delta f_n = +0.48\%$		$\Delta\zeta_n = -35.94\%$	
2	15.505	0.9520	15.435	0.8298
	$\Delta f_n = +0.46\%$		$\Delta\zeta_n = +14.73\%$	
3	16.490	0.8072	16.319	1.0104
	$\Delta f_n = +1.05\%$		$\Delta\zeta_n = -20.11\%$	
4	17.647	1.0927	17.418	1.4823
	$\Delta f_n = +1.31\%$		$\Delta\zeta_n = -26.28\%$	
5	20.791	0.8886	20.679	1.1544
	$\Delta f_n = +0.54\%$		$\Delta\zeta_n = -23.02\%$	
6	22.834	1.2149	22.159	1.1693
	$\Delta f_n = +3.05\%$		$\Delta\zeta_n = +3.90\%$	
7	24.343	1.1922	25.363	1.3191
	$\Delta f_n = -4.02\%$		$\Delta\zeta_n = -9.62\%$	
8	25.657	0.9408	24.199	1.0395
	$\Delta f_n = +6.03\%$		$\Delta\zeta_n = -9.50\%$	
9	26.453	1.2938	26.294	1.5583
	$\Delta f_n = +0.60\%$		$\Delta\zeta_n = -16.97\%$	
12	39.810	1.4791	40.176	2.0702
	$\Delta f_n = -0.91\%$		$\Delta\zeta_n = -28.55\%$	
13	40.783	1.4751	43.292	1.6487
	$\Delta f_n = -5.80\%$		$\Delta\zeta_n = -10.53\%$	
14	47.337	0.9206	46.900	1.6770
	$\Delta f_n = +0.93\%$		$\Delta\zeta_n = -45.11\%$	
15	49.379	1.4705	49.999	3.0676
	$\Delta f_n = -1.24\%$		$\Delta\zeta_n = -52.06\%$	
16	53.502	1.3341	53.381	2.4089
	$\Delta f_n = +0.23\%$		$\Delta\zeta_n = -44.62\%$	
20	67.664	0.5387	67.590	0.5573
	$\Delta f_n = +0.11\%$		$\Delta\zeta_n = -3.33\%$	
21	68.826	0.8645	68.750	1.2700
	$\Delta f_n = +0.11\%$		$\Delta\zeta_n = -31.93\%$	

Mode	HS_WN_01		HS_WN_01 [26]	
	f_n [Hz]	ζ_n [%]	f_n [Hz]	ζ_n [%]
22	71.851	2.2703	72.166	1.8760
	$\Delta f_n = -0.44\%$		$\Delta\zeta_n = +21.02\%$	
24	76.995	3.6178	81.018	3.0466
	$\Delta f_n = -4.97\%$		$\Delta\zeta_n = +18.75\%$	
28	94.460	0.5357	94.701	0.6435
	$\Delta f_n = -0.25\%$		$\Delta\zeta_n = -16.76\%$	
29	97.647	2.0228	97.458	2.4663
	$\Delta f_n = +0.19\%$		$\Delta\zeta_n = -17.98\%$	
31	102.979	1.4612	102.146	2.1364
	$\Delta f_n = +0.81\%$		$\Delta\zeta_n = -31.60\%$	
32	106.797	1.7788	106.544	1.7431
	$\Delta f_n = +0.24\%$		$\Delta\zeta_n = +2.05\%$	
33	115.631	0.9794	115.050	1.4856
	$\Delta f_n = +0.51\%$		$\Delta\zeta_n = -34.07\%$	
34	121.004	1.5384	120.952	1.4795
	$\Delta f_n = +0.04\%$		$\Delta\zeta_n = +3.98\%$	
35	125.561	1.0482	125.377	1.2535
	$\Delta f_n = +0.15\%$		$\Delta\zeta_n = -16.38\%$	
36	128.642	0.5398	128.984	0.5204
	$\Delta f_n = -0.27\%$		$\Delta\zeta_n = +3.73\%$	
37	132.071	0.6409	132.213	0.7157
	$\Delta f_n = -0.11\%$		$\Delta\zeta_n = -10.45\%$	
38	137.460	0.5088	137.581	0.8660
	$\Delta f_n = -0.09\%$		$\Delta\zeta_n = -41.25\%$	
40	149.358	0.7425	149.674	0.6797
	$\Delta f_n = -0.21\%$		$\Delta\zeta_n = +9.23\%$	
41	151.342	1.1129	151.894	0.9359
	$\Delta f_n = -0.36\%$		$\Delta\zeta_n = +18.91\%$	
42	156.364	0.8149	156.916	1.0311
	$\Delta f_n = -0.35\%$		$\Delta\zeta_n = -20.97\%$	

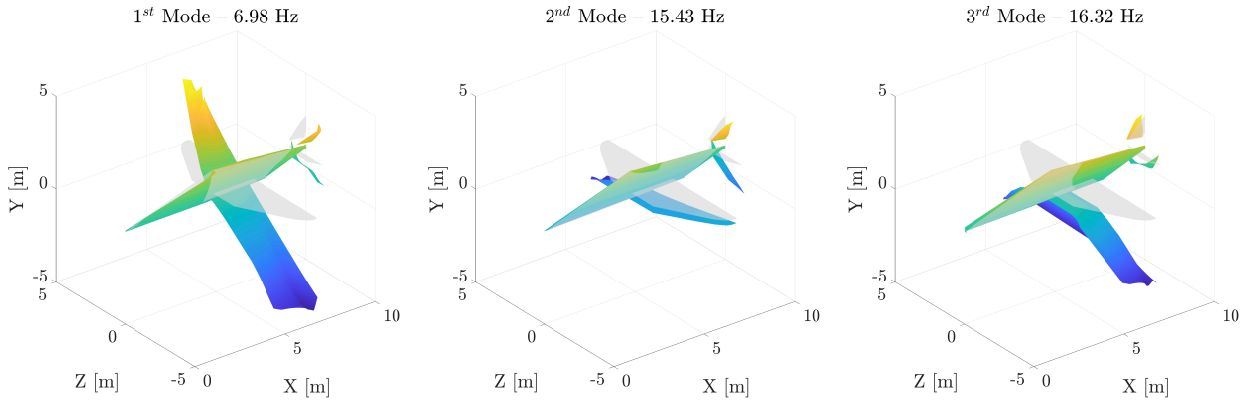


Figure 6 – BAE Systems Hawk T1A aircraft: $\boldsymbol{\phi}_n$ of the first three modes identified via MIMO iLF at 0.4 V (reference case). Retrieved from [26].

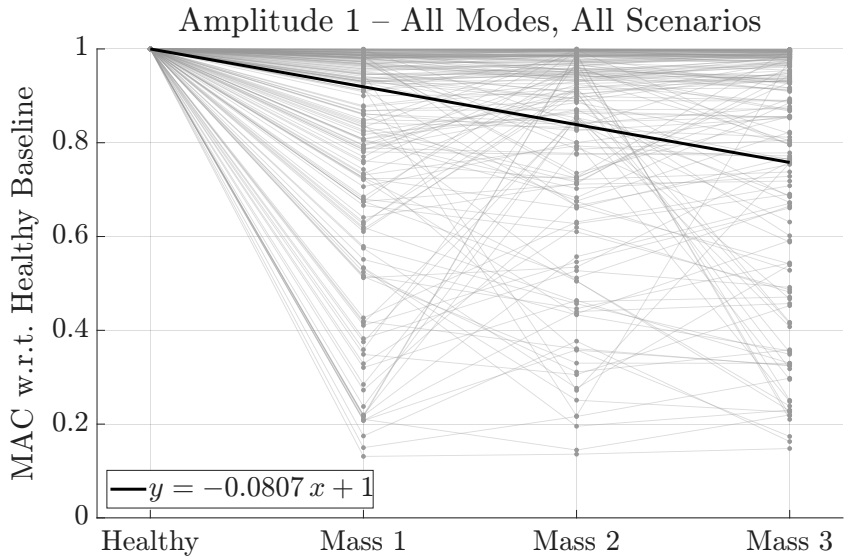


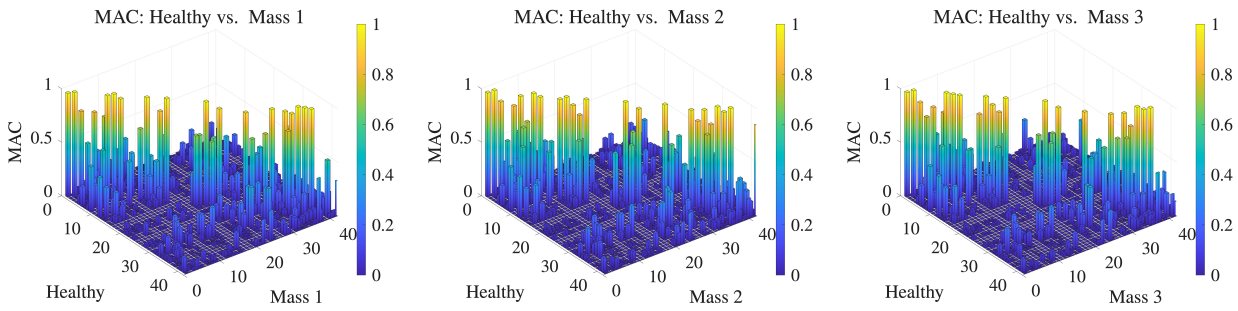
Figure 7 – BAE Systems Hawk T1A aircraft: MAC values with respect to the healthy baseline for all 31 identified modes, pooled across all six damage scenarios and all three damage levels (Amplitude 1).

increasing damage severity. This aggregate trend motivates the identification of individual modes whose response is strictly monotonic — and hence more reliable as damage indicators — under the criterion of Equation (4).

3.2 Single-scenario analysis: SW_CTE

The remainder of this section focuses on the SW_CTE scenario (cases 2–4 in Table 1), which provides three incremental damage levels at a fixed location and is therefore the most controlled configuration to evaluate the monotonicity criterion. Figure 8 presents the MAC matrices between the healthy baseline and each of the three damage states (M1, M2, M3), displayed as three-dimensional bar plots with mode index on both axes. These matrices illustrate the complete pairwise $\boldsymbol{\phi}_n$ correlation structure between healthy and damaged configurations.

The diagonal MAC values degrade progressively from M1 to M3. Although many modes retain near-unity values at M1, a subset exhibit measurable reductions that become more pronounced at M2 and M3. The off-diagonal entries remain uniformly low, confirming that mode tracking via Equation (3) is reliable and that no mode-pairing ambiguity has occurred. Figure 9 overlays the tracked MAC values per-mode with the constrained regression for the SW_CTE scenario, providing a view of the damage response relative to the trend.



(a) Healthy vs M1 (b) Healthy vs M2 (c) Healthy vs M3

Figure 8 – BAE Systems Hawk T1A aircraft: MAC matrices between the healthy baseline and each of the three damage levels (M1, M2, M3) for the SW_CTE scenario (Amplitude 1). Diagonal entries represent mode-to-mode correlation; off-diagonal entries indicate cross-correlation. Empty bars correspond to modes not identified in one of the two states.

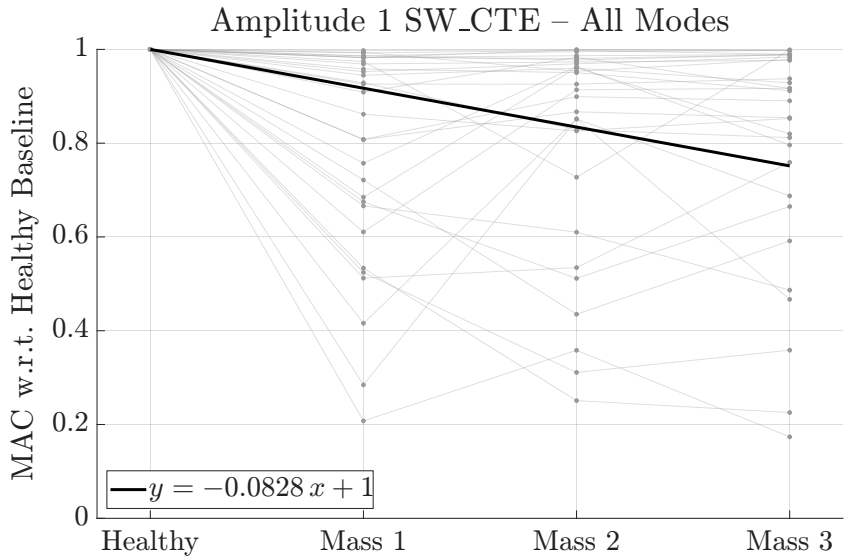


Figure 9 – BAE Systems Hawk T1A aircraft: MAC values with respect to the healthy baseline for all 31 identified modes, SW_CTE scenario, all three damage levels at 0.1 V.

Applying the strict monotonicity criterion of Equation (4) to the SW_CTE scenario identifies four damage indicator modes. Table 3 reports the natural frequencies, damping ratios, and tracked MAC values for these modes across all four structural states (Healthy, M1, M2, M3).

Table 3 – BAE Systems Hawk T1A aircraft: damage indicator modes for the SW_CTE scenario, all four structural states (Amplitude 1). Only modes satisfying the strict monotonic MAC decrease criterion of Equation (4) are listed.

Mode	**Healthy**		**M1**			**M2**			**M3**		
	f_n [Hz]	ζ_n [%]	f_n [Hz]	ζ_n [%]	MAC	f_n [Hz]	ζ_n [%]	MAC	f_n [Hz]	ζ_n [%]	MAC
29	97.647	2.02	96.638	1.11	0.67	98.279	2.42	0.61	98.636	2.64	0.49
32	106.797	1.78	107.269	1.64	0.96	107.185	1.72	0.95	107.241	1.81	0.91
35	125.561	1.05	125.524	1.26	0.93	125.686	1.30	0.83	125.582	0.96	0.81
41	151.342	1.11	150.582	1.26	0.53	149.299	2.92	0.25	149.958	0.69	0.23

Figure 10 presents the mode shapes $\boldsymbol{\phi}_n$ of the four damage indicator modes, computed from the identification of the healthy baseline. The spatial character of each $\boldsymbol{\phi}_n$ is qualitatively consistent with its MAC behaviour under damage.
Mode 29 (97.6 Hz) exhibits a spatially distributed vibration pattern across both wings and the fuse-

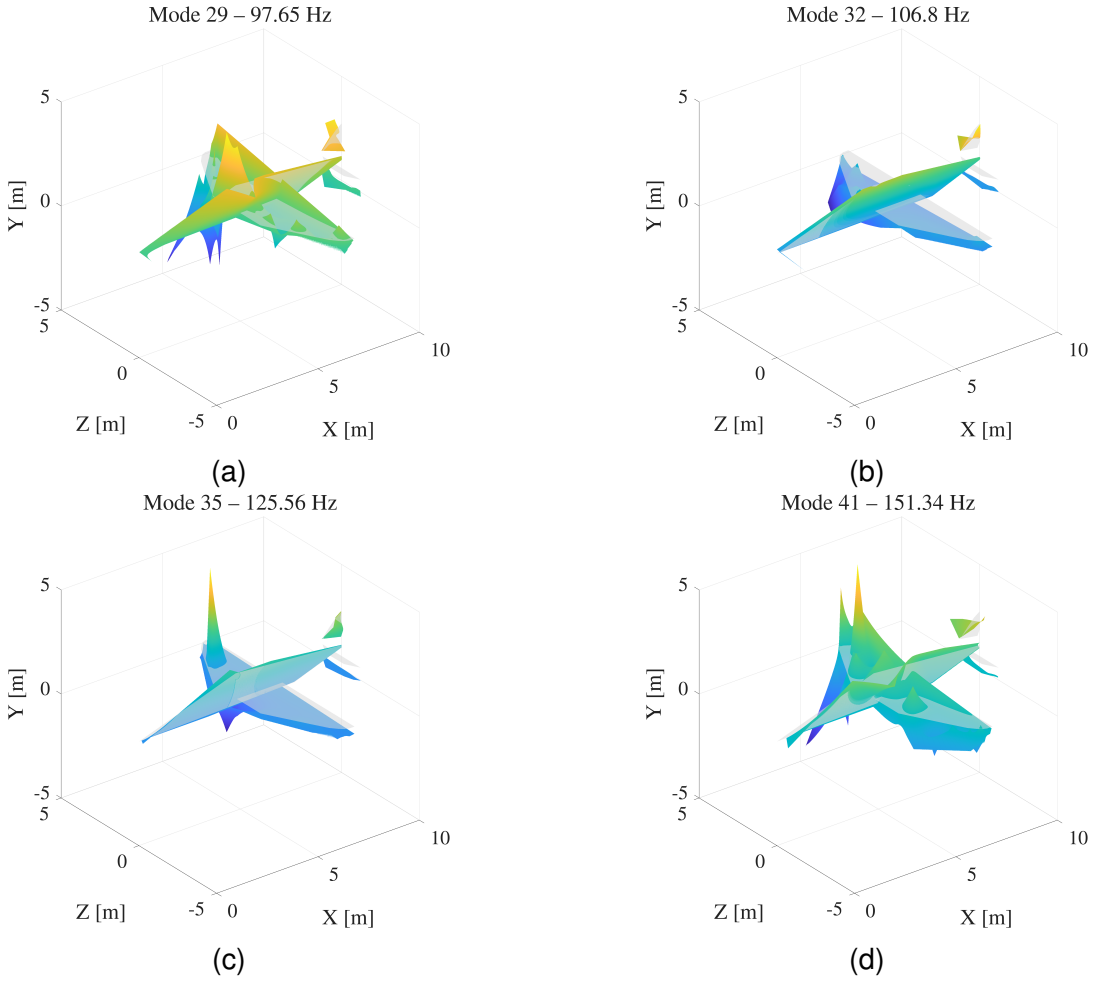


Figure 10 – BAE Systems Hawk T1A aircraft: mode shapes $\boldsymbol{\phi}_n$ of the four damage indicator modes (healthy state, SW_CTE scenario). Grey surface: undeformed configuration; coloured surface: deformed $\boldsymbol{\phi}_n$ normalised to unit maximum displacement.

lage, with pronounced out-of-plane content in the fuselage mid-section and the region of the starboard tip of the wing; this distributed and complex spatial character is consistent with the relatively low absolute MAC values (0.6662 at M1) and their substantial degradation to 0.4866 at M3. Mode 32 (106.8 Hz) is dominated by a predominantly smooth span-wise bending of the wing surfaces with limited participation from the fuselage and tail surfaces; the higher initial MAC (0.9581) and its controlled, steady decrease to 0.9117 at M3 reflect the cleaner and more spatially coherent nature of this mode. Mode 35 (125.6 Hz) displays two large vertical-response regions near the wing root and tip; the monotonic MAC reduction from 0.9287 to 0.8118 traces a clear damage-sensitive trajectory for this mode. Mode 41 (151.3 Hz) is the most spatially complex of the four, with large-amplitude, multidirectional vibration components that involve the fuselage, wings, and vertical stabiliser simultaneously; accordingly, it exhibits the largest degradation of MAC in the four indicators, dropping from 0.5336 at M1 to 0.2255 at M3, consistent with high sensitivity to localised structural modifications.
Figure 11 presents the tracked MAC progression of the four damage indicator modes as a function of damage level, together with the constrained regression curve fitted to the full set of modes for reference. The figure confirms the strict monotonic decrease of all four modes, with modes 29 and 41 showing the most pronounced degradation, and modes 32 and 35 tracking damage more slowly. The regression slope of -0.0828 characterises the average MAC sensitivity of the full mode set to increasing mass addition, whilst the damage indicator modes span a range of individual sensitivities that can be used differentially for both detection and preliminary severity assessment.

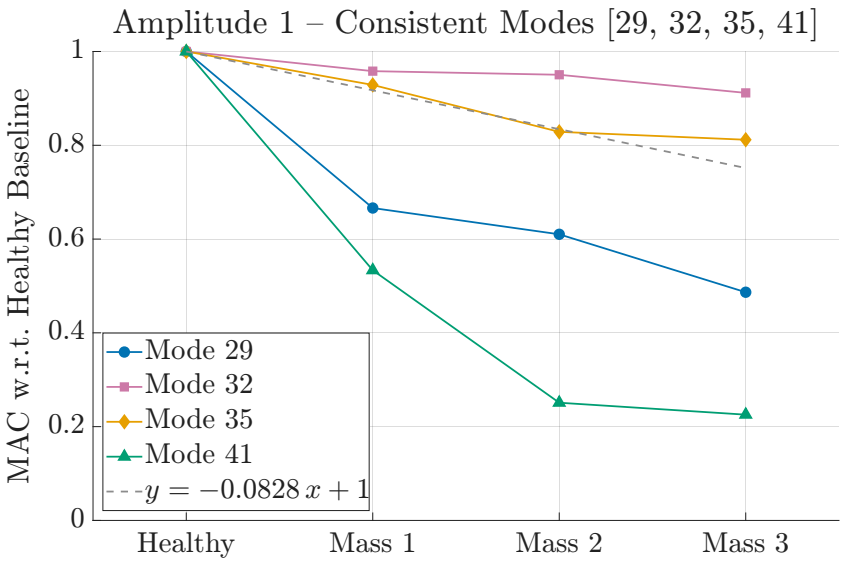


Figure 11 – BAE Systems Hawk T1A aircraft: MAC progression of the four damage indicator modes (SW_CTE scenario, Amplitude 1) as a function of damage level.

4. Discussion

The results presented in Section 3. confirm that $\boldsymbol{\phi}_n$, condensed via the MAC, constitute a viable damage indicator for a full-scale airframe under controlled laboratory conditions. Nevertheless, there are two observations that require specific attention.

The first point concerns the consistency of the aggregate damage response across scenarios. The constrained regression slopes of -0.0807 (all scenarios considered, Figure 7) and -0.0828 (SW_CTE scenario, Figure 9) are numerically close, differing by less than 0.3% (more precisely, 0.0021) in absolute terms. This near-equivalence indicates that no single damage location dominates the aggregate MAC trend, and that the average sensitivity of the mode set to increasing mass addition is stable across the six scenarios considered. The implication is practical: a regression-based severity metric calibrated on one damage location may retain predictive value when other locations are affected, which is a necessary, if not sufficient, condition for the generalisation of the detection strategy to unknown damage positions.

The second observation concerns the selection of damage indicator modes. The four modes identified under the strict monotonicity criterion of Equation (4) — at 97.6, 106.8, 125.6, and 151.3 Hz — span a range of individual MAC sensitivities that can be exploited differentially. Modes 29 and 41, which exhibit the highest degradation (approximately 0.4866 and 0.2255 in M3, respectively), are the most responsive to localised mass addition in SW_CTE and therefore better suited to early detection. Modes 32 and 35, whose MAC decreases are more gradual and spatially coherent, are better candidates for severity tracking, as their response remains interpretable throughout the complete progression of damage, without saturation. The spatial character of each $\boldsymbol{\phi}_n$, as shown in Figure 10, is consistent with this hierarchy: the more globally distributed modes are more sensitive to localised modifications, whilst the spatially coherent modes respond more predictably.

The practical extension of this framework to in-service monitoring introduces challenges that are absent from the controlled GVT setting. Under operational conditions, the excitation is unknown, the noise floor is elevated, and environmental and operational conditions (EOCs) — temperature, boundary condition variations, aerodynamic loading — introduce noise-like effects on modal parameters. Of the three classical modal parameters, ω_n is the most sensitive to EOC-induced variability, whilst ζ_n is rarely reliable as a standalone indicator owing to its dependence on non-structural factors [8]. $\boldsymbol{\phi}_n$ occupy an intermediate position: they are less susceptible to temperature-driven stiffness changes than ω_n, but their estimation under output-only conditions introduces statistical uncertainty that must be quantified before detection thresholds can be established. This uncertainty is traceable and can be quantified. The scatter associated with ζ_n estimates in OMA is well documented to be substantially larger than that of ω_n and $\boldsymbol{\phi}_n$ [32], and the confidence intervals for the MAC estimates can be analyti-

cally propagated within the stochastic subspace identification framework [33]. This is consistent with the observation that ζ_n discrepancies in the present identification are substantially larger than those in ω_n or $\boldsymbol{\phi}_n$, as reported in Tables 2 and 3.

These considerations do not preclude the application of mode shape-based SHM to operational structures of comparable complexity. Modal tracking under ambient excitation is routinely demonstrated in civil structures and infrastructures subject to significant operational and environmental variability, including masonry bridges [6], heritage structures subject to soil–structure interaction, such as the Leaning Tower of Pisa [34], and multi-span concrete bridges undergoing controlled progressive damage scenarios [35]. Cable-stayed and suspension bridges subject to aeroelastic excitation under wind loading represent a further relevant class: long-term monitoring campaigns on structures such as the Hardanger Bridge [36], which combine geometric nonlinearity, fluid–structure coupling, and continuously varying operational loads, have demonstrated reliable modal tracking and damage-sensitive feature extraction. The aerodynamic environment of a jet trainer in service is more severe and less stationary than that of a bridge. Nevertheless, the methodological precedent is well established in these domains: the mode shape ($\boldsymbol{\phi}_n$) correlation can be maintained as a damage indicator under substantial operational variability when appropriate baseline normalisation and compensation for environmental and operational conditions are applied.

The present study operates entirely within the linear response regime at a fixed excitation amplitude, and all damage states consist of mass additions rather than fatigue cracks or debonding. Extending the conclusions to realistic in-service damage modes requires validation on datasets that include genuine structural degradation and that span multiple environmental states.

5. Conclusions and Future Work

This work has demonstrated vibration-based airframe health monitoring on a full-scale BAE Systems Hawk T1A jet trainer using mode shape correlation as the primary damage indicator. Modal parameters were extracted via the iLF across 19 MIMO ground vibration test configurations that covered six damage scenarios and three incremental mass levels, with the healthy baseline serving as the reference state against which all damaged configurations were compared.

The main findings are as follows:

- The iLF correctly resolves the global dynamics of the airframe at 0.1 V, with natural frequency agreement within 1% for 25 of 31 identified modes relative to the 0.4 V reference.
- The constrained regression slopes of -0.0807 (all scenarios pooled) and -0.0828 (SW_CTE) differ by less than 0.3%, confirming that the aggregate MAC sensitivity to damage is consistent across all locations.
- The four modes at 97.6, 106.8, 125.6, and 151.3 Hz satisfy the strict monotonicity criterion and constitute reliable damage indicators for the SW_CTE scenario.
- The tracked MAC values range from 0.9581 (mode 32, M1) to 0.2255 (mode 41, M3), covering a wide sensitivity range across the four indicator modes.
- Modes 29 and 41 are, based on all these findings, the ones best suited for early detection; modes 32 and 35 provide a more gradual and interpretable severity response.

Future work will extend the analysis to all damage scenarios and amplitude levels, and implement a complementary damage-localisation method based upon the MAC-based detection strategy demonstrated here. The longer-term objective is to extend the framework to operational structures, addressing the environmental and operational condition variability that characterises in-service airframe monitoring.

Contact Author Email Address

Gabriele Dessena: gdessena@ing.uc3m.es

Acknowledgement

This work is supported by the Madrid Government (*Comunidad de Madrid*, Spain) under the Multiannual Agreement with the Universidad Carlos III de Madrid (IA_aCTRl-CM-UC3M). The first author is supported by grant JDC2024-055593-I funded by MICIU/AEI /10.13039/501100011033 and by ESF+. The Department of Aerospace Engineering at UC3M has been accredited as Unit of Excellence "María de Maeztu", a distinction awarded by the Spanish State Research Agency for the period 01/01/2026-31/12/2031. The authors would like to express their utmost gratitude to the members of the Laboratory of Verification and Validation (LVV) at the University of Sheffield for making the BAE Systems Hawk T1A database publicly available.

Copyright Statement

The authors confirm that they, and/or their company or organization, hold copyright on all of the original material included in this paper. The authors also confirm that they have obtained permission, from the copyright holder of any third party material included in this paper, to publish it as part of their paper. The authors confirm that they give permission, or have obtained permission from the copyright holder of this paper, for the publication and distribution of this paper as part of the ICAS proceedings or as individual off-prints from the proceedings.

References

[1] Filippo De Florio. *Airworthiness*. Elsevier, 2011.

[2] Kostas Bardis, Nicolas P. Avdelidis, Clemente Ibarra-Castanedo, Xavier P. V. Maldague, and Henrique Fernandes. Advanced diagnostics of aircraft structures using automated non-invasive imaging techniques: A comprehensive review. *Applied Sciences*, 15:3584, 3 2025.

[3] William R. Hendricks. The aloha airlines accident — a new era for aging aircraft. In S.N. Atluri, S.G. Sampath, and P. Tong, editors, *International Symposium on Structural Integrity of Aging Airplanes, Springer Series in Computational Mechanics*, pages 153–165. Springer Berlin Heidelberg, 1991.

[4] Andres Rytter. *Vibrational Based inspection of Civil Engineering Structures*. PhD thesis, Aalborg University, 1993.

[5] Wei Fan and Pizhong Qiao. Vibration-based damage identification methods: A review and comparative study. *Structural Health Monitoring*, 10:83–111, 1 2011.

[6] Marco Civera, Giulia Calamai, and Luca Zanotti Fragonara. System identification via fast relaxed vector fitting for the structural health monitoring of masonry bridges. *Structures*, 30:277–293, 4 2021.

[7] Martina Modesti, Cristina Gentilini, Antonio Palermo, Edwin Reynders, and Geert Lombaert. A two-step procedure for damage detection in beam structures with incomplete mode shapes. *Journal of Civil Structural Health Monitoring*, 8 2024.

[8] Edwin Reynders, Rik Pintelon, and Guido De Roeck. Uncertainty bounds on modal parameters obtained from stochastic subspace identification. *Mechanical Systems and Signal Processing*, 22:948–969, 5 2008.

[9] Sisi Zhang, Max Käding, Marc Wenner, Martin Claßen, and Steffen Marx. Structural health monitoring (shm) on a long semi-integral high-speed railway bridge (hsrb) under different traffic loads. *Engineering Structures*, 325:119445, 2 2025.

[10] Silvia Vettori, Emilio Di Lorenzo, Bart Peeters, and Eleni Chatzi. Assessment of alternative covariance functions for joint input-state estimation via gaussian process latent force models in structural dynamics. *Mechanical Systems and Signal Processing*, 213:111303, 5 2024.

[11] Lechen Li, Adrian Brügger, Raimondo Betti, Zhenzhong Shen, Lei Gan, and Hao Gu. A cepstrum-informed neural network for vibration-based structural damage assessment. *Computers & Structures*, 306:107592, 1 2025.

[12] Ambroise Cadoret, Enora Denimal-Goy, Jean-Marc Leroy, Jean-Lou Pfister, and Laurent Mevel. Damage detection and localization method for wind turbine rotor based on operational modal analysis and anisotropy tracking. *Mechanical Systems and Signal Processing*, 224:111982, 2 2025.

[13] Georgios Dadoulis, George D Manolis, Konstantinos Katakalos, Kosmas Dragos, and Kay Smarsly. Damage detection in lightweight bridges with traveling masses using machine learning. *Engineering Structures*, 322:119216, 2025.

[14] Yuanqiang Ren, Jiaxuan Li, Shenfang Yuan, Lei Qiu, Limin Gao, and Mingyu Lu. An enhanced probability signal construction based on-line damage imaging method for aircraft structures under service environment. *Aerospace Science and Technology*, 168:110787, 1 2026.

[15] Peter Cawley. Structural health monitoring: Closing the gap between research and industrial deployment. *Structural Health Monitoring*, 17:1225–1244, 9 2018.

[16] Tedja Verhulst, David Judt, Craig Lawson, Yongmann Chung, Osama Al-Tayawe, and Geoff Ward. Review for state-of-the-art health monitoring technologies on airframe fuel pumps. *International Journal of Prognostics and Health Management*, 13:1–20, 6 2022.

[17] Yue Liu, Weifeng Long, Yugang Chen, and Haifeng Hu. Nonlinear vibration characteristics and damage detection method of blade with breathing fatigue crack. *Aerospace Science and Technology*, 155:109715, 2024.

[18] Wentao Zhang, Kuan Lu, Yichi Zhang, Jin Chen, Dapeng Fu, Yang Yang, and Chao Fu. A comprehensive study on dynamic responses of the whole aero-engine system and design of variable stiffness brackets. *Aerospace Science and Technology*, 159:110010, 4 2025.

[19] Fang Fang, Lei Qiu, Shenfang Yuan, and Yuanqiang Ren. Dynamic probability modeling-based aircraft structural health monitoring framework under time-varying conditions: Validation in an in-flight test simulated on ground. *Aerospace Science and Technology*, 95:105467, 12 2019.

[20] Richard S. Pappa, George H. James, and David C. Zimmerman. Autonomous modal identification of the space shuttle tail rudder. *Journal of Spacecraft and Rockets*, 35:163–169, 3 1998.

[21] Gabriele Dessena, Marco Civera, Luca Zanotti Fragonara, Dmitry I. Ignatyev, and James F. Whidborne. A loewner-based system identification and structural health monitoring approach for mechanical systems. *Structural Control and Health Monitoring*, 2023:1–22, 4 2023.

[22] Edwin Reynders, Jeroen Houbrechts, and Guido De Roeck. Fully automated (operational) modal analysis. *Mechanical Systems and Signal Processing*, 29:228–250, 5 2012.

[23] Bart Peeters and Guido De Roeck. One-year monitoring of the z24-bridge: environmental effects versus damage events. *Earthquake Engineering & Structural Dynamics*, 30:149–171, 2 2001.

[24] Charles R. Farrar, Nikolaos Dervilis, and Keith Worden. The past, present and future of structural health monitoring: An overview of three ages. *Strain*, 61, 2 2025.

[25] James Wilson, Max D. Champneys, Matt Tipuric, Robin Mills, David J. Wagg, and Timothy J. Rogers. Multiple-input, multiple-output modal testing of a hawk t1a aircraft: a new full-scale dataset for structural health monitoring. *Structural Health Monitoring*, pages 1–23, 12 2024.

[26] Gabriele Dessena and Marco Civera. Improved tangential interpolation-based multi-input multi-output modal analysis of a full aircraft. *European Journal of Mechanics - A/Solids*, 110:105495, 3 2025.

[27] Gabriele Dessena, Marco Civera, Andrés Marcos, Bernardino Chiaia, and Oscar E. Bonilla-Manrique. Multiple input tangential interpolation-driven damage detection of a jet trainer. *Aerospace Science and Technology*, 168:111032, 1 2026.

[28] Gabriele Dessena, Marco Civera, Andrés Marcos, Bernardino Chiaia, and Oscar E. Bonilla-Manrique. Vibration-based damage detection and localisation on a trainer jet aircraft wing. In Spiros Pantelakis, Andreas Strohmayer, and Gustavo Alonso, editors, *The 15th EASN International Conference on "Innovation in Aviation & Space Towards Sustainability Today & Tomorrow"*, 44. MDPI, 2026.

[29] Tarek Berghout. Military training aircraft structural health monitoring leveraging an innovative biologically inspired feedback mechanism for neural networks. *Machines*, 13:179, 2 2025.

[30] Peter Avitabile. *Modal Testing: A Practitioner's Guide*. John Wiley & Sons, 2017.

[31] Randall J. Allemang and David L. Brown. A correlation coefficient for modal vector analysis. In *Proceedings of the 1st International Modal Analysis Conference*, pages 110–116. Union College, 1982.

[32] Carlo Rainieri and Giovanni Fabbrocino. *Operational Modal Analysis of Civil Engineering Structures*. Springer New York, 2014.

[33] Szymon Greś, Michael Döhler, and Laurent Mevel. Uncertainty quantification of the modal assurance criterion in operational modal analysis. *Mechanical Systems and Signal Processing*, 152:107457, 5 2021.

[34] Laura Vignali, Anna de Falco, Kristof Maes, and Edwin Reynders. Long-term dynamic monitoring of the leaning tower of Pisa. In Michael Döhler, Adrien Mélot, and Manuel Aenlle López, editors, *Proceedings of the 11th International Operational Modal Analysis Conference (IOMAC 2025)*, pages 674 – 681. International Group of Operational Modal Analysis, 5 2025.

[35] Larisa Garcia-Ramonda, Simona Bogoevska, Yves Reuland, Panagiotis Martakis, Vasilis Dertimanis, and Eleni Chatzi. Ponte moesa campagnola: A bridge benchmark for structural identification under controlled damage progression. *Journal of Structural Engineering*, 151, 12 2025.

[36] Aksel Fenerci, Ole Øiseth, and Anders Rønnquist. Long-term monitoring of wind field characteristics and dynamic response of a long-span suspension bridge in complex terrain. *Engineering Structures*, 147:269–284, 9 2017.